

EMRRG: Efficient Fine-Tuning Pre-trained X-ray Mamba Networks for Radiology Report Generation [★]

Mingzheng Zhang¹, Jinfeng Gao¹, Dan Xu¹, Jiangrui Yu¹, Yuhan Qiao¹,
Lan Chen², Jin Tang¹, and Xiao Wang¹

¹ School of Computer Science and Technology, Anhui University, Hefei 230601, China

² School of Electronic and Information Engineering, Anhui University, Hefei 230601, China

Abstract. X-ray image-based medical report generation (MRG) is a pivotal area in artificial intelligence that can significantly reduce diagnostic burdens for clinicians and patient wait times. Existing MRG models predominantly rely on Large Language Models (LLMs) to improve report generation, with limited exploration of pre-trained vision foundation models or advanced fine-tuning techniques. Mainstream frameworks either avoid fine-tuning or utilize simplistic methods like LoRA, often neglecting the potential of enhancing cross-attention mechanisms. Additionally, while Transformer-based models dominate vision-language tasks, non-Transformer architectures, such as the Mamba network, remain underexplored for medical report generation, presenting a promising avenue for future research. In this paper, we propose EMRRG, a novel X-ray report generation framework that fine-tunes pre-trained Mamba networks using parameter-efficient methods. Specifically, X-ray images are divided into patches, tokenized, and processed by an SSM-based vision backbone for feature extraction, with Partial LoRA yielding optimal performance. An LLM with a hybrid decoder generates the medical report, enabling end-to-end training and achieving strong results on benchmark datasets. Extensive experiments on three widely used benchmark datasets fully validated the effectiveness of our proposed strategies for the X-ray MRG. The source code of this paper will be released on https://github.com/Event-AHU/Medical_Image_Analysis.

Keywords: X-ray Medical Report Generation · Mamba Network · Parameter Efficient Fine-Tuning

1 Introduction

X-ray based medical report generation (MRG) [32] represents a pivotal application of artificial intelligence in healthcare, utilizing sophisticated AI models to generate high-fidelity diagnostic reports from radiographic images autonomously. This technology holds significant promise for mitigating clinical workload burdens, reducing diagnostic delays, and facilitating the operational integration of AI systems into routine clinical workflows. While AI performance has demonstrated remarkable progress, MRG systems continue to underperform relative to the diagnostic acumen of experienced clinicians, attributable to persistent technical and systemic limitations. The challenging

[★] Corresponding author: Xiao Wang (xiaowang@ahu.edu.cn)

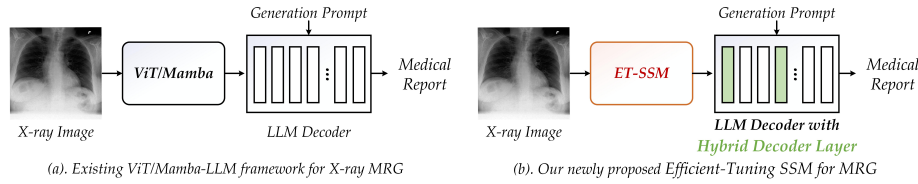


Fig. 1: Comparison between (a). Existing ViT/Mamba-LLM framework for X-ray medical report generation; (b). Our newly proposed Efficient-Tuning based SSM for MRG.

issues include image interpretation, data annotation, heterogeneity issues, consistency and standardization of reports, diversity and variability of diseases, interpretability of algorithms, etc.

To address these challenges, some researchers resort to pre-trained foundation models, such as Llama [11], Qwen [1], to further augment the overall performance. Specifically, Chen et al. propose the R2Gen [5] framework based on the Transformer network, and many subsequent works [6, 41, 46] are designed by following this framework. Wang et al. propose a novel X-ray medical report generation framework called R2GenCSR [41] that adopts the Mamba architecture as its backbone and mines contextual samples to guide large language models for high-quality report generation. Wang et al. introduce the MambaXray-VL [43], which adopts the Mamba as the vision encoder and the large language model as the text decoder.

Despite these great progresses, current MRG systems are still limited by the following issues: 1). Most existing Medical Report Generation (MRG) models focus primarily on leveraging Large Language Models (LLMs) [46] to enhance report generation capabilities. Yet, few works explore the use of pre-trained vision foundation models to improve overall performance, particularly through lightweight fine-tuning of these models. 2). Mainstream frameworks that employ LLMs for report generation typically either avoid fine-tuning altogether or apply simple strategies such as LoRA [15] for fine-tuning the large models. While these approaches can yield decent results, they primarily exploit the self-attention mechanism and overlook the potential of expanding cross-attention capabilities. 3). Transformer-based models have recently dominated various vision-language tasks, however, exploration of non-Transformer architectures remains notably insufficient. Investigating how to leverage cutting-edge non-Transformer models, e.g., the Mamba network [12], to enhance the quality of medical report generation is a promising and underexplored direction.

In this paper, we propose a novel X-ray report generation framework by efficiently tuning the pre-trained Mamba networks, termed EMRRG. As shown in Fig. 1, the key insight of this paper lies in exploring novel parameter-efficient approaches to fine-tune pre-trained non-Transformer models and better adapt them to LLMs to enhance the quality of generated medical reports. Specifically, given an X-ray image, we first partition it into image patches and map them into tokens. These tokens are then fed into an efficiently tuned SSM (State Space Model)-based vision backbone for feature extraction. During this process, we investigate multiple fine-tuning paradigms and find that Partial LoRA achieves the best performance. Subsequently, we employ an

LLM equipped with a hybrid decoder layer as the decoder network to generate the corresponding medical report. The entire framework supports end-to-end training and achieves strong experimental results across multiple mainstream benchmark datasets. The detailed network architectures can be found in Fig. 2.

To sum up, the main contributions of this paper can be summarized as the following three aspects:

- 1). We propose a novel Mamba-based X-ray medical report generation framework, termed EMRRG, based on parameter efficient fine-tuning.
- 2). We introduce a hybrid decoder layer augmented large language model (LLM) for accurate report generation.
- 3). Extensive experiments on three benchmark datasets (i.e., IU X-ray [8], MIMIC [20], CheXpert Plus Dataset [3]) fully validated the effectiveness of our proposed strategies for the radiology report generation.

2 Related Work

2.1 Mamba Network

State Space Model (SSM) [44] serves as the foundation for Mamba, functioning as a linear-complexity approach for modeling long-range dependencies. Evolving from the original SSM to the Structured State Space sequence model (S4) [12], and subsequently to Mamba and Mamba2 [7], these architectures have continuously advanced in efficiency and theoretical grounding. Mamba [12] introduces data-dependent selective state updates and hidden state expansion, enabling efficient sequence modeling with linear time complexity. Its strong performance across diverse domains highlights its ability to maintain computational efficiency while achieving accuracy comparable to Transformer-based models. In computer vision, Mamba has been adapted into the Vision Mamba (ViM) [54] architecture. ViM employs pure Mamba layers with bidirectional scanning, achieving efficient and scalable visual representation learning. This linear-complexity design makes ViM suitable for large-scale pretraining and multi-modal integration. However, as model scales grow, fine-tuning such architectures efficiently becomes increasingly challenging, motivating research into Parameter-Efficient Fine-Tuning (PEFT) strategies.

2.2 Parameter Efficient Fine-Tuning

Parameter-Efficient Fine-Tuning (PEFT) aims to adapt large pre-trained models to downstream tasks while updating only a small subset of parameters [21]. Typical PEFT methods fall into three categories: partial-based, addition-based, and prompt-based approaches [10]. In contrast to the Transformer domain, PEFT research for Mamba remains relatively limited [53]. Recent efforts have begun exploring selective and structured tuning within Mamba architectures. SDLoRA [10] combines selective dimension tuning with Low-Rank Adaptation (LoRA), updating only specific channels and states within SSM modules while applying LoRA to linear projections. Selective Visual Prompting (SVP) [50], designed for Vision Mamba (ViM) [54], introduces a lightweight

dual-path prompting mechanism Cross-Prompting for shared information propagation and Inner-Prompting for layer-specific adaptation. Similarly, Partial LoRA [53] applies LoRA selectively to Mamba’s linear layers, improving performance with minimal parameter overhead. Despite these advances, PEFT for Mamba in high-resolution medical imaging remains underexplored, motivating our investigation into efficient fine-tuning frameworks for radiographic report generation.

2.3 X-ray Report Generation

X-ray report generation has evolved through several architectural paradigms, including CNN-based, RNN-based, and Transformer-based frameworks [41]. Early works such as Li et al. [22] integrated CNNs for visual feature extraction with RNNs for sequential text generation, while Jing et al. [19] introduced an LSTM-based pipeline [13] that predicts pathological findings before report composition. The introduction of Transformers led to major breakthroughs, Chen et al. [6] utilized self-attention to generate detailed diagnostic descriptions, and Wang et al. [42] enhanced vision-language pre-training by adapting Vision Transformers (ViT) [9] with masked autoencoding objectives on medical images. Recent developments have emphasized clinical relevance and interpretability. DCL [23] integrates dynamic graph reasoning to encode domain knowledge; RGRG [35] combines lesion detection with region-guided text generation; and HERGen [38] models temporal dependencies among historical reports. The latest methods, such as R2GenGPT [46] and R2GenCSR [41], incorporate large language models (LLMs) or Mamba-based visual backbones to enhance contextual reasoning and feature discriminability. In summary, the field has progressed from foundational CNN/RNN frameworks to Transformer-based and Mamba-based architectures that emphasize efficiency, temporal reasoning, and clinical alignment. Building on this evolution, our work integrates the Mamba backbone with PEFT mechanisms to achieve efficient and accurate X-ray report generation.

3 Methodology

In this section, we will first give an overview of our proposed EMRRG model, then, we will dive into the details of the Partial LoRA and the hybrid decoder layers. Finally, we introduce the loss function used in this work.

3.1 Overview

As shown in Fig. 2, we propose a novel framework for X-ray report generation. This framework comprises the efficient fine-tuning of pre-trained Mamba networks and the introduction of a hybrid decoder layer augmented large language models (LLMs) to facilitate accurate report generation. Compared to the Transformer, SSM models achieve higher computational efficiency owing to their sub-quadratic time complexity. Therefore, building upon the SSM architecture, we propose ET-SSM (Efficient-Tuning based SSM). This approach utilizes Partial LoRA to fine-tune the intermediate features X of the Mamba model, while applying traditional LoRA to the input projection layer. This

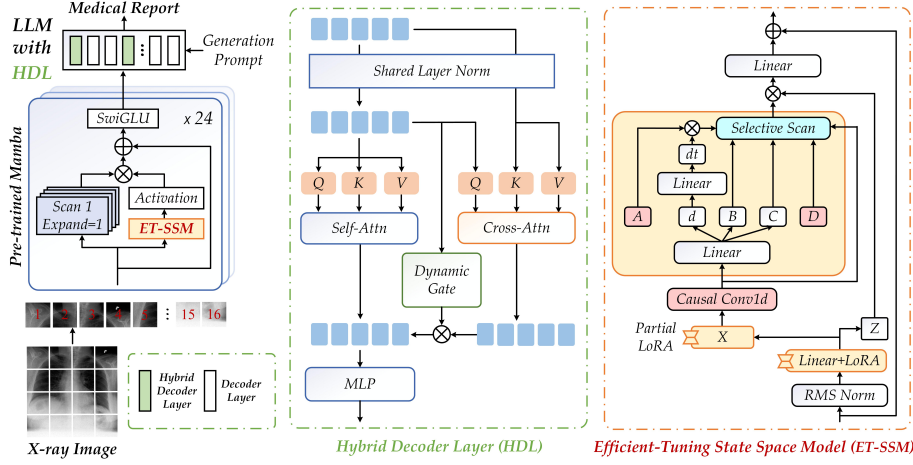


Fig. 2: An overview of our proposed X-ray medical report generation framework by efficient tuning Mamba networks, termed EMRRG.

strategy enhances the quality of input representations at the feature extraction source and further improves training efficiency. More importantly, during the report generation stage, we replace part of the standard decoder layers with hybrid decoder layers incorporating a cross-attention mechanism, which demonstrates superior performance compared to the widely used self-attention mechanism. Theoretically, the cross-attention mechanism allows text embeddings to dynamically extract relevant information from the uncompressed visual features, guided by the instruction to generate a diagnostic report. In the context of medical reporting, this enables the model to focus on key regions within the X-ray image (e.g., lesion sites), thereby producing more accurate and clinically relevant descriptions while avoiding interference from extraneous details.

3.2 Input Encoding

In this paper, we denote the X-ray image as $I \in \mathbb{R}^{192 \times 192 \times 3}$, we initially partition it into non-overlapping image patches $P_i \in \mathbb{R}^{16 \times 16 \times 3}$, $i = \{1, 2, \dots, N\}$ and project them into visual tokens $T_i \in \mathbb{R}^{1024}$, $i = \{1, 2, \dots, N\}$ using a convolutional layer with a kernel size of 16×16 . Here, N is 144 when the input image resolution is set to $3 \times 192 \times 192$. The visual tokens are subsequently fed into the Vim backbone network for feature extraction. This architecture achieves a significantly lower computational complexity of $\mathcal{O}(N)$ compared to the $\mathcal{O}(N^2)$ of the widely adopted Transformer. The core component of Vim is the Mamba block, a specific variation of the State Space Model (SSM), which enables this efficiency.

3.3 Efficient-Tuning SSM

This work addresses the characteristic presence of numerous intermediate features with distinct properties (e.g., X , Z , dt , B , C) in Mamba networks by proposing an effi-

cient fine-tuning strategy that integrates localized adaptation with global optimization. Although LoRA, as an architecture-agnostic parameter-efficient fine-tuning method, can be directly applied to Mamba, conventional implementations compress all intermediate features into a single low-rank subspace, thereby ignoring their inherent differences. As shown in the right part of Fig. 2, to tackle this limitation, we introduce the $\text{LoRA}_P(X)$ [53] method, which applies LoRA adaptations selectively to only a portion of the weights in linear layers based on the structure of the output features, achieving more refined parameter updates.

Furthermore, we employ conventional LoRA fine-tuning on the input projection layer to enhance the quality of input representations at the source of feature extraction. This approach not only strengthens the discriminative power of features subsequently processed by the selective scan mechanism but also facilitates synergistic modeling between the X and Z pathways. This comprehensive and hierarchical fine-tuning framework significantly improves the model’s efficiency in the chest X-ray medical report generation task.

3.4 LLM with Hybrid Decoder

The hybrid decoder layer constitutes the core architectural component of our LLM. As illustrated in the middle section of Fig. 2, this layer builds upon and extends the standard decoder layer. To ensure seamless integration of cross-attention within the decoder architecture, we conceptualize it as complementary to self-attention: whereas self-attention aggregates contextual information from preceding textual tokens, cross-attention simultaneously extracts relevant visual context from visual tokens.

The cross-attention module operates in parallel with self-attention, with its output being integrated back into the textual embeddings via a skip connection. A key innovation in this integration pathway is the introduction of a dynamic gating mechanism, which adaptively modulates the fused output prior to its incorporation into the main representation. This gating approach serves dual purposes: it effectively mitigates potential information interference while concurrently enhancing training stability. In the subsequent section, we provide a comprehensive elaboration of both the computational pipeline for cross-attention and the architectural design of the dynamic gate.

Cross-attention. The hybrid decoder layer takes hidden states and visual tokens as input. Following prior works [33, 51], these inputs are first normalized through a shared layer normalization. The normalized outputs then undergo two parallel attention mechanisms: while all hidden states participate in self-attention, only text-derived queries from the self-attention layer are utilized for cross-attention with visual tokens. For conciseness, attention head dimensions are omitted in our description. We denote the textual query by $\mathbf{Q}_t \in \mathbb{R}^{n \times d}$, where n is the number of text tokens and d is the hidden dimension. Let the (normalized) visual features be $\mathbf{V}_s \in \mathbb{R}^{m \times d}$, with m visual tokens. The cross-attention output $\mathbf{X}' \in \mathbb{R}^{n \times d}$ is computed by a multi-head cross-attention (MHCA) module as

$$\mathbf{X}' = \text{MHCA}(\mathbf{Q}_t, W_k \mathbf{V}_s, W_v \mathbf{V}_s), \quad (1)$$

where $\text{MHCA}(q, k, v)$ denotes multi-head cross-attention with query q , key k , and value v . W_k and W_v are learnable linear projections that align visual features to the key and value spaces, respectively.

Dynamic gate with warm-up. To mitigate potential noise introduced by cross-attention outputs X' into pretrained LLMs, we employ a dynamic gating mechanism with warm-up initialization. While existing approaches typically use learnable scalar gates [11], these static assignments fail to account for varying visual context requirements across different tokens, as demonstrated by divergent attention patterns [56]. Our method generates token-wise gating values g_t through a linear layer followed by tanh activation, enabling adaptive fusion of visual features into textual embeddings. Following [33], we initialize a warm-up scalar to zero to stabilize early training phases, allowing the model to learn optimal integration weights throughout the multimodal alignment process gradually. The output of the cross-attention module is then integrated into the textual embedding X_t via a gated residual update:

$$\mathbf{X}_t \leftarrow \mathbf{X}_t + (\mathbf{X}' \odot g_d) \cdot g_s, \quad (2)$$

where \odot denotes the element-wise (Hadamard) product, and g_d and g_s are gating factors that modulate the contribution of the cross-attention output. This gated residual connection updates the text-specific component of the hidden states, while the self-attention branch provides complementary contextual refinement across tokens.

3.5 Loss Function

In this paper, we adopt the negative log-likelihood as the loss function, i.e.,

$$\mathcal{L}_{NLL} = - \sum_{i=1}^T \log p_\theta(y_i | \text{Prompt}, [y_1, \dots, y_{i-1}]), \quad (3)$$

where θ represents the trainable parameters, T is the number of words predicted by the Large Language Model, and Prompt is the instruction used in our experiments, i.e., "Generate a comprehensive and detailed diagnosis report for this chest X-ray image."

4 Experiments

4.1 Datasets and Evaluation Metric

In this article, three public benchmark datasets are adopted for experimental validation and analysis, including IU-Xray [8], MIMIC-CXR [20], and CheXpert Plus [3] datasets. A brief introduction to these datasets is given below.

- **IU X-ray Dataset** [8] published in 2016, is one of the most frequently used publicly available medical image datasets for the generation of medical reports. It contains 7,470 images and 3,955 radiology reports; each report is associated with either a frontal view image or both frontal and lateral view images. Each report is divided into four sections: Indication, Comparison, Findings, and Impression. For a fair comparison, we used the

same dataset split protocol as R2GenGPT [46], dividing the dataset into training, testing, and validation sets with a ratio of 7:1:2.

- **MIMIC-CXR Dataset** [20] is one of the largest publicly available chest X-ray datasets, containing free-text radiology reports. These records from 2011-2016 include 377,110 radiographic images and 227,835 radiology reports collected from 65,379 patients at the Beth Israel Deaconess Medical Center Emergency Department in Boston, Massachusetts. For fair comparison, we used the same dataset split protocol as R2GenGPT, with 270,790 samples for training the model, and 2,130 and 3,858 samples for validation and testing sets, respectively.
- **CheXpert Plus Dataset** [3] is a new radiology dataset designed to enhance the scale, performance, robustness, and fairness of deep learning models in the field of radiology. This dataset includes 223,228 chest X-rays (in DICOM and PNG formats), 187,711 corresponding radiology reports (de-identified and parsed into 11 sections), de-identified demographic data from 64,725 patients, 14 chest pathology labels, and RadGraph [17] annotations. For a fair comparison, we followed the dataset split protocol used in R2GenCSR [41], which adopted Findings as the ground truth and split the training/validation/testing subsets based on the ratio 7:1:2. The training subset contains 40,463 samples, the validation subset contains 5,780 samples, and the testing subset contains 11,562 samples.

For evaluation metrics, we adopt natural language metrics and clinical metrics to evaluate our generated X-ray reports. For the natural language metrics, we choose BLEU [31], ROUGE-L [26], METEOR [2], and CIDEr [37]. For the clinical metrics, i.e., *Precision*, *Recall*, and *F1-measure*, the formula can be formally defined as:

$$Precision = \frac{TP}{TP + FP}, \quad (4)$$

$$Recall = \frac{TP}{TP + FN}, \quad (5)$$

$$F1 = \frac{2 \times P \times R}{P + R} \quad (6)$$

where TP (True Positive) refers to instances that are correctly identified as positive, FP (False Positive) denotes cases incorrectly labeled as positive when they are actually negative (also known as a Type I error), and FN (False Negative) represents instances incorrectly classified as negative despite being positive (referred to as a Type II error). The F1 Score serves as a harmonic mean of Precision and Recall, providing a balanced measure that accounts for both the accuracy of positive predictions and the ability to capture all relevant positive cases, without favoring one metric over the other.

4.2 Implementation Details

We tested the model’s performance on three widely used public benchmark datasets. On the IU-Xray [8] dataset, we set the maximum training epochs to 30 and the batch size to 20. The visual encoder used was Vim [54], loaded with pre-trained weights from [43], while the large language model was Qwen-1.5-1.8B [1], with max_length set to 60 and a validation frequency of 1, meaning we validated after each training epoch.

On the MIMIC-CXR [20] and CheXpert Plus [3] datasets, we set the maximum training epochs to 6 and the batch size to 18. The visual encoder remained unchanged, while the large language model used was Llama2-7B [36], with `max_length` set to 100 and a validation frequency of 0.5, meaning we validated at both the end of each training cycle and after the training was complete. When implementing the LoRA_P(X) methodology for fine-tuning, specifically during the application of LoRA to partial weights of the `in_proj` layer, the rank parameter r was configured to 32. For the language model, four hybrid decoder layers are distributed within the LLM’s decoder layers at indices [0, 8, 16, 24]. More details can be found in our source code.

Table 1: Comparison with SOTA on the **NLG Metrics**. The symbol \dagger indicates that we follow the R2Gen annotation using *Findings* and evaluate with our method, as their report modifies the ground truth to an *Impression* concatenated with *Findings*. The best result is highlighted in bold, and the second-best result is underlined.

Dataset	Method	Publication	BLEU-1	BLEU-2	BLEU-3	BLEU-4	ROUGE-L	METEOR	CIDEr
IU X-Ray	R2Gen [5]	EMNLP 2020	0.470	0.304	0.219	0.165	0.371	0.187	-
	R2GenCMN [6]	ACL-IJCNLP 2021	0.475	0.309	0.222	0.170	0.375	0.191	-
	METransformer [45]	CVPR 2023	0.483	0.322	0.228	0.172	0.380	0.192	0.435
	DCL [23]	CVPR 2023	-	-	-	0.163	<u>0.383</u>	0.193	0.586
	R2GenGPT \dagger [46]	Meta Radiology 2023	0.465	0.299	0.214	0.161	0.376	0.219	0.542
	PromptMRG [18]	AAAI 2024	0.401	-	-	0.098	0.160	0.281	-
	Med-LMM [28]	ACM MM 2024	-	-	-	0.168	0.381	0.209	0.427
	SILC [27]	IEEE TMI 2024	0.472	<u>0.321</u>	<u>0.234</u>	<u>0.175</u>	0.379	0.192	0.368
	KIA [52]	COLING 2025	0.501	<u>0.325</u>	<u>0.240</u>	<u>0.183</u>	0.375	0.207	<u>0.559</u>
MIMIC-CXR	EMRRG	Ours	0.487	0.325	0.222	0.167	0.385	0.226	0.476
	R2Gen [5]	EMNLP 2020	0.353	0.218	0.145	0.103	0.277	0.142	-
	R2GenCMN [6]	ACL-IJCNLP 2021	0.353	0.218	0.148	0.106	0.278	0.142	-
	METransformer [45]	CVPR 2023	0.386	0.250	0.169	0.124	<u>0.291</u>	0.152	0.362
	DCL [23]	CVPR 2023	-	-	-	0.109	0.284	0.150	<u>0.281</u>
	R2GenGPT \dagger [46]	Meta Radiology 2023	0.408	0.256	0.174	0.125	0.285	0.167	0.244
	PromptMRG [18]	AAAI 2024	0.398	-	-	0.112	0.268	0.157	-
	Med-LMM [28]	ACM MM 2024	-	-	-	<u>0.128</u>	0.289	0.161	0.265
	AdaMatch-Cyclic [4]	ACL 2024	0.379	0.235	0.154	0.106	0.286	0.163	-
	GIT-CXR [34]	arXiv 2025	0.403	0.254	<u>0.215</u>	<u>0.136</u>	<u>0.311</u>	0.161	-
CheXpert Plus	EMRRG	Ours	0.407	0.256	<u>0.175</u>	0.125	0.288	0.164	0.239
	R2Gen [5]	EMNLP 2020	0.301	0.179	0.118	0.081	0.246	0.113	0.077
	R2GenCMN [6]	ACL-IJCNLP 2021	0.321	0.195	0.128	0.087	0.256	0.127	0.102
	XProNet [39]	ECCV 2022	0.364	0.225	0.148	0.100	0.265	<u>0.146</u>	0.121
	ORGan [14]	ACL 2023	0.320	0.196	0.128	0.086	0.261	0.135	0.107
	R2GenGPT [46]	Meta Radiology 2023	0.361	0.224	<u>0.149</u>	<u>0.101</u>	<u>0.266</u>	0.145	<u>0.123</u>
	ASGMD [48]	ESWA 2024	0.267	0.149	0.094	0.063	0.220	0.094	0.044
	Token-Mixer [49]	IEEE TMI 2024	0.378	<u>0.231</u>	0.153	0.091	0.262	0.135	0.098
	PromptMRG [18]	AAAI 2024	0.326	0.174	-	0.095	0.222	0.121	0.044
	R2GenCSR [41]	arXiv 2024	0.364	0.225	0.148	0.100	0.265	0.146	0.121
	EMRRG	Ours	<u>0.375</u>	<u>0.232</u>	<u>0.153</u>	<u>0.104</u>	<u>0.273</u>	<u>0.152</u>	<u>0.167</u>

4.3 Comparison on Public Benchmarks

• **Results on IU X-ray Dataset.** As shown in Table 1, our EMRRG exhibits excellent performance on the IU X-ray dataset. To elaborate further, the EMRRG model is at the SOTA level on BLEU-2 (B2) and ROUGEL (R) metrics with scores of 0.325 and 0.385, respectively. Furthermore, we attained the second-best results on the BLEU-1 (B1) and

Table 2: Comparison of the **CE Metrics** on MIMIC-CXR dataset.

Method	Publication	MIMIC-CXR		
		Precision	Recall	F1
R2Gen [5]	EMNLP 2020	0.333	0.273	0.276
METransformer [45]	CVPR 2023	0.364	0.309	0.311
KIUT [16]	CVPR 2023	0.371	0.318	0.321
DCL [23]	CVPR 2023	0.471	0.352	0.373
CoFE [24]	ECCV 2024	0.489	0.370	0.405
HERGen [38]	ECCV 2024	0.415	0.301	0.317
SILC [27]	IEEE TMI 2024	0.457	0.337	0.330
OaD [25]	IEEE TMI 2024	0.364	0.382	0.372
GIT-CXR [34]	arXiv 2025	0.349	0.403	0.336
EMRRG	Ours	0.421	0.372	0.395

Table 3: Comparison of the **CE Metrics** on CheXpert Plus dataset.

Method	Publication	CheXpert Plus		
		Precision	Recall	F1
R2Gen [5]	EMNLP 2020	0.318	0.200	0.181
R2GenCMN [6]	ACL 2021	0.329	0.241	0.231
XProNet [39]	ECCV 2022	0.314	0.247	0.259
R2GenGPT [46]	Meta-Rad. 2023	0.315	0.244	0.260
Zhu et al. [55]	MICCAI 2023	0.217	0.308	0.205
PromptMRG [18]	AAAI 2024	0.258	0.265	0.281
Token-Mixer [49]	IEEE TMI 2024	0.309	0.270	0.288
EMRRG	Ours	0.341	<u>0.273</u>	0.272

METEOR (M) metrics, with corresponding scores of 0.487 and 0.226, respectively. This result demonstrates that our method achieves performance comparable to other report generation approaches. However, on some other metrics, such as BLEU-3 (B3), BLEU-4 (B4), and CIDEr (C), our method does not achieve comparable performance. This reflects the need to improve the generalization of our method on other datasets.

• **Results on MIMIC-CXR Dataset.** As shown in Table 1, our method also demonstrates outstanding performance on the MIMIC-CXR dataset, and achieves the most comparable level in several common indicators (e.g., BLEU-1, BLEU-2, BLEU-3, and METEOR). Specifically, our method outperforms R2GenGPT on the ROUGE-L metric and also achieves favorable performance on the BLEU-4 metric. In the CIDEr metric, our model achieved a score of 0.239, indicating that EMRRG still has room for improvement. Furthermore, as shown in Table 2, our method also demonstrates comparable performance on the CE metric; our scores on Precision (P), Recall (R), and F1-score (F1) are 0.421, 0.372, and 0.395, respectively.

• **Results on CheXpert Plus Dataset.** As shown in Table 1 and Table 3, our model EMRRG achieves state-of-the-art performance across nearly all evaluation metrics. These include NLG evaluation metrics and CE evaluation metrics. In detail, for the NLG metrics, our scores on BLEU-4, ROUGE-L, METEOR, and CIDEr are 0.104, 0.273, 0.152, and 0.167, respectively. For the CE metrics, our scores on Precision (P), Recall (R), and F1-score (F1) are 0.341, 0.273, and 0.272, respectively. These experimental results fully demonstrate the superior performance of our model.

4.4 Ablation Study

• **Component Analysis.** In Table 5, for the SSM, LoRA_P(X) indicates fine-tuning the intermediate feature X of the SSM using the Partial LoRA method. For the LLM, L2+LoRA represents fine-tuning Llama2 with the conventional LoRA method; L2+HDL represents replacing part of the original decoder layers in Llama2 with hybrid decoder layers. B1–B4 are short for BLEU-1 to BLEU-4, respectively, and R-L, M, and C are short for ROUGE-L, METEOR, and CIDEr, respectively.

From the results presented in Table 5, under the condition of keeping the LLM operations unchanged, the LoRA_P(X) method achieves performance close to full fine-

Table 4: Runtime Efficiency on the CheXpert Plus Dataset using **Mainstream Medical Report Generation Algorithms**. Min is short for minutes. The Param listed in this table denotes the parameters that need to be tuned in the training phase.

Index	Algorithm	Publish	Encoder	Decoder	Time (min)	Param (M)
#01	TIMER [47]	CHIL23	Transformer	Transformer	26.5	79.28
#02	CvT2DistilGPT2 [30]	AIM23	Transformer	GPT2	13.93	128.00
#03	ORGan [14]	ACL23	CNN	Transformer	46.66	67.50
#04	Zhu et al. [55]	MICCAI23	Transformer	Transformer	10.03	85.95
#05	CAMANet [40]	IEEE JBH23	Swin-Former	Transformer	23.08	43.22
#06	ASGMD [48]	ESWA24	ResNet-101	Transformer	87.37	277.41
#07	Token-Mixer [49]	IEEE TMI23	ResNet-50	Transformer	17.54	104.34
#08	PromptMRG [18]	AAAI24	ResNet-101	Bert	108.45	219.92
#09	R2GenGPT [46]	Meta-Rad.23	Swin-Transformer	Llama2	77.80	90.90
#10	R2GenCSR [41]	arXiv24	VMamba	Llama2	31.20	91.70
#11	Wang et al. [43]	arXiv24	ViT	Llama2	10.82	358.80
#12	MambaXray-VL [43]	CVPR2025	MambaXray-VL	Llama2	50.66	57.31
#13	EMRRG	Ours	MambaXray-VL	Llama2	26.84	1.32

Table 5: Component analysis of the key method in our framework on the IU X-ray dataset. It is stated as follows: full fine-tuning (FT), Llama2 (L2), hybrid decoder layer (HDL). The best result is highlighted in bold, and the second-best result is underlined.

Index	SSM		LLM			IU X-ray						
	FT	LoRA _P (X)	L2	L2+LoRA	L2+HDL	B1	B2	B3	B4	R-L	M	C
#01	✓	✗	✓	✗	✗	0.480	0.322	0.226	0.175	0.383	0.215	0.478
#02	✓	✗	✗	✓	✗	0.473	0.311	0.216	0.171	0.384	0.210	0.483
#03	✓	✗	✗	✗	✓	0.489	<u>0.324</u>	0.231	0.182	0.391	<u>0.219</u>	0.490
#04	✗	✓	✓	✗	✗	0.475	0.309	0.211	0.161	0.372	0.208	0.464
#05	✗	✓	✗	✓	✗	0.471	0.313	0.216	0.158	0.374	0.210	0.461
#06	✗	✓	✗	✗	✓	0.487	0.325	0.222	0.167	<u>0.385</u>	0.226	0.476

tuning (FT) across multiple metrics. Notably, for certain metrics, the LoRA_P(X) method even outperforms FT. As demonstrated by comparing rows #02 and #05, the LoRA_P(X) method performs comparably to FT on BLEU-3 and METEOR metrics, while surpassing FT on the BLEU-2 metric. When maintaining consistent SSM operations, the Llama2+HDL approach demonstrates superior performance over both standard Llama2 and Llama2+LoRA across nearly all evaluation metrics.

Overall, while the combination of the FT method with Llama2+HDL achieves optimal results on multiple metrics, and the LoRA_P(X) method with Llama2+HDL only attains optimal performance on BLEU-2 and METEOR metrics, our proposed EMRRG framework still maintains performance close to the full parameter fine-tuning approach. Importantly, it should be emphasized that our EMRRG framework requires training only 2.3% of the parameters compared to full fine-tuning methods, resulting in significantly higher training efficiency than full parameter fine-tuning approaches.

Table 6: NLG Metrics of EMRRG Framework Components Fine-tuned with LoRA and Partial LoRA on IU X-ray Dataset. The best result is highlighted in bold, and the second-best result is underlined.

Setting	BLEU-1	BLEU-2	BLEU-3	BLEU-4	ROUGE-L	METEOR	CIDEr
LoRA(Llama2)	0.479	0.320	0.233	0.177	0.386	<u>0.212</u>	0.489
LoRA(embedding)	0.463	0.302	0.218	0.167	0.379	0.207	0.530
LoRA(x_proj)	0.457	0.301	<u>0.226</u>	0.162	0.383	0.205	0.473
LoRA(dt_proj)	0.458	0.300	0.212	0.161	0.378	0.203	0.485
LoRA(in_proj)	0.444	0.288	0.205	0.152	0.368	0.194	0.431
LoRA(out_proj)	0.456	0.297	0.211	0.156	0.374	0.199	0.451
LoRA _p (Z)	0.466	0.302	0.213	0.163	0.381	0.204	0.467
LoRA _p (dt)	0.458	0.299	0.221	0.157	<u>0.387</u>	0.197	0.484
LoRA _p (B)	0.462	0.307	0.208	0.165	0.384	0.201	0.472
LoRA _p (C)	0.473	0.303	0.217	0.154	0.379	0.209	0.466
LoRA _p (X)	0.485	<u>0.311</u>	0.223	<u>0.169</u>	0.388	0.216	0.474

• **Analysis of Different Tuning Settings.** As shown in Table 6, the results of fine-tuning different components using the LoRA method indicate that fine-tuning the parameters of the decoder Llama2 achieves superior performance, obtaining optimal scores on the BLEU-2, BLEU-3, and BLEU-4 metrics. This inspires further in-depth research on the text decoder, specifically by replacing part of the original decoder layers with hybrid decoder layers. Moreover, from the fine-tuning results of intermediate feature networks with various attributes in Mamba (such as X, Z, dt, B, C, etc., see Figure 2) using the Partial LoRA method, LoRA_P(X) attains the best performance across multiple metrics, thereby laying the experimental foundation for our proposed ET-SSM framework.

• **Efficiency Analysis** From the perspective of running efficiency, we test these models on a server with A800 GPUs (80GB). Note that we set the batch size as large as possible to make full use of the GPU memory. As a result, we can find that MSAT [40] and XProNet [39] are the first two algorithms that only need 5.72 and 6.3 minutes for the testing subset. R2Gen [6], PromptMRG [18], and VLCI [29] are relatively slow and need more than 100 minutes on the testing subset of the CheXpert Plus dataset. From the Table 1 to Table 4, we can find that Our EMRRG has demonstrated remarkably strong performance in terms of both computational efficiency and predictive accuracy, yielding surprisingly favorable outcomes. It fully validated the efficiency of our proposed framework for the X-ray image based medical report generation.

4.5 Visualization

As shown in Fig. 3, we present several examples to demonstrate the effectiveness of our proposed EMRRG model for X-ray image-based report generation. For specific X-ray images, we compare the ground-truth reports with those generated by the MambaXray-VL model and our EMRRG model. The selected X-ray images include different views and a variety of conditions, allowing for a more comprehensive and ob-

X-ray Image	Ground Truth	MambaXray-VL	EMRRG (Ours)
	Cardiomedastinal silhouette is within normal limits. The lungs are clear without evidence of focal consolidation. There are degenerative changes of the shoulder, bilaterally, with surgical rotator cuff fixation pins in place.	Cardiomedastinal silhouette is within normal limits. The lungs are clear without evidence of focal consolidation or pleural effusion. The visualized osseous structures are unremarkable, degenerative changes are seen in the thoracic spine.	Cardiomedastinal silhouette is within normal limits. The lungs are clear without evidence of focal consolidation or pleural effusion or pneumothorax. Degenerative changes are seen in the thoracic spine and shoulder bilaterally with degenerative changes.
	A single portable AP view of the chest demonstrates a right-sided subclavian vein catheter with tip at the cavalatrial junction. The lung volumes are low. No definite areas of consolidation are evident. The soft tissues and bones are unremarkable.	A single portable AP view of the chest demonstrates a right-sided subclavian vein catheter with tip at the cavalatrial junction. No evidence of pneumothorax, pulmonary edema or pleural effusions. The bones and soft tissues are unremarkable.	A single portable AP view of the chest demonstrates a right-sided subclavian vein catheter with tip at the cavalatrial junction. Low lung volumes are demonstrated. There is no evidence of focal consolidation, pulmonary edema or pneumothorax. The soft tissues and bones are unremarkable.
	There is redemonstration of a right internal jugular tunneled central venous catheter, terminating in the distal superior vena cava. The lungs remain clear. There is no evidence of pleural effusion. The cardiomedastinal silhouette is within normal limits. Regional osseous structures appear unremarkable.	The cardiomedastinal silhouette and pulmonary vascularity are within normal limits. There is no evidence of focal consolidation, pleural effusion or pneumothorax. Soft tissues and osseous structures are unremarkable.	There has been redemonstration of a right internal jugular tunneled central venous catheter with the tip in the distal superior vena cava. The cardiomedastinal silhouette is within normal limits. The lungs are clear. There is no evidence of pleural effusion. The visualized osseous structures are unremarkable.
	Interval intubation with the endotracheal tube tip 3.7 cm above the carina. Interval placement of a left internal jugular sheath and Swan-Ganz catheter with the tip in the main pulmonary artery. Interval removal of a left internal jugular central venous catheter. Decreased bilateral trace pleural effusions and mild pulmonary edema. Persistent bilateral opacities, likely atelectasis versus consolidation. No pneumothorax.	Interval placement of a right internal jugular central venous catheter with the tip in the superior vena cava. Persistent bilateral opacities likely atelectasis versus consolidation. Decreased bilateral pleural effusions. Mild pulmonary edema. Cardiomedastinal silhouette is unchanged.	Interval intubation with the endotracheal tube tip approximately 3 cm above the carina. Interval placement of a left internal jugular Swan-Ganz catheter with the tip in the main pulmonary artery. Stable appearance of a small left pleural effusion and bilateral opacities which may represent atelectasis or consolidation. No pneumothorax.

Fig. 3: Comparison of generated reports on the CheXpert dataset. Yellow highlights indicate sentences in the **MambaXray-VL** report matching the ground truth, cyan highlights denote matching sentences in our **EMRRG** report, and pink highlights represent matches shared by both models.

jective evaluation. For a more intuitive visualization, we have highlighted the parts that match the ground truth. The yellow highlighted area represents the part of the report generated by the MambaXray-VL model that matches the ground truth, while the cyan highlighted area corresponds to the part of the report generated by the EMRRG model that matches the ground truth. The pink-highlighted area indicates the portion of the report generated by both models that matches the ground truth. It is evident that the reports produced by our EMRRG model contain a greater amount of content consistent with the ground truth compared to those generated by MambaXray-VL, confirming the superior accuracy and effectiveness of our approach.

4.6 Limitation Analysis

This paper provides an Efficient model for the X-ray image based medical report generation. The LLMs evaluated in this work focus on 7B, which is hardware-friendly, and the LLMs with more parameters are not discussed due to the limited computational resources. On the other hand, due to computational resource constraints, we neither fine-tuned all components within the Mamba architecture nor identified an optimal subset of fine-tuned components.

5 Conclusion

In this paper, we propose an efficient architecture for X-ray image-based medical report generation. This architecture achieves enhanced performance through two

methodological advancements: 1) parameter-efficient fine-tuning of the Mamba structure within the MambaXray-VL framework using the LoRA_P(X) method, and 2) partial replacement of conventional decoder layers with Hybrid Decoder Layers in large language models. The effectiveness of our proposed EMRRG model was validated through rigorous comparative evaluations against state-of-the-art medical report generation algorithms on the IU X-ray, MIMIC-CXR, and CheXpert Plus datasets.

References

1. Bai, J., Bai, S., Chu, Y., et al.: Qwen technical report. arXiv preprint arXiv:2309.16609 (2023)
2. Banerjee, S., Lavie, A.: Meteor: An automatic metric for mt evaluation with improved correlation with human judgments. In: Proceedings of the acl workshop on intrinsic and extrinsic evaluation measures for machine translation and/or summarization. pp. 65–72 (2005)
3. Chambon, P., Delbrouck, J.B., Sounack, T., et al.: CheXpert plus: Augmenting a large chest x-ray dataset with text radiology reports, patient demographics and additional image formats. arXiv preprint arXiv:2405.19538 (2024)
4. Chen, W., Shen, L., Lin, J., Luo, J., Li, X., Yuan, Y.: Fine-grained image-text alignment in medical imaging enables explainable cyclic image-report generation. In: Proceedings of the 62nd Annual Meeting of the Association for Computational Linguistics (Volume 1: Long Papers). pp. 9494–9509 (2024)
5. Chen, Z., Song, Y., Chang, T.H., Wan, X.: Generating radiology reports via memory-driven transformer. arXiv preprint arXiv:2010.16056 (2020)
6. Chen, Z., Song, Y., Chang, T.H., Wan, X.: Generating radiology reports via memory-driven transformer. In: Proceedings of the 2020 Conference on Empirical Methods in Natural Language Processing (EMNLP). pp. 1439–1449. Association for Computational Linguistics, Online (Nov 2020)
7. Dao, T., Gu, A.: Transformers are ssms: Generalized models and efficient algorithms through structured state space duality. arXiv preprint arXiv:2405.21060 (2024)
8. Demner-Fushman, D., Kohli, M.D., Rosenman, M.B., Shooshan, S.E., Rodriguez, L., Antani, S., Thoma, G.R., McDonald, C.J.: Preparing a collection of radiology examinations for distribution and retrieval. Journal of the American Medical Informatics Association **23**(2), 304–310 (2016)
9. Dosovitskiy, A., Beyer, L., Kolesnikov, A., Weissenborn, D., Houlsby, N.: An image is worth 16x16 words: Transformers for image recognition at scale (2020)
10. Galim, K., Kang, W., Zeng, Y., Koo, H.I., Lee, K.: Parameter-efficient fine-tuning of state space models. arXiv preprint arXiv:2410.09016 (2024)
11. Grattafiori, A., Dubey, A., Jauhri, A., Pandey, A., Kadian, A., Al-Dahle, A., Letman, A., Mathur, A., Schelten, A., Vaughan, A., et al.: The llama 3 herd of models. arXiv preprint arXiv:2407.21783 (2024)
12. Gu, A., Dao, T.: Mamba: Linear-time sequence modeling with selective state spaces. arXiv preprint arXiv:2312.00752 (2023)
13. Hochreiter, S., Schmidhuber, J.: Long short-term memory. Neural Computation (1997)
14. Hou, W., Xu, K., Cheng, Y., Li, W., Liu, J.: ORGAN: Observation-guided radiology report generation via tree reasoning. In: Proceedings of the 61st Annual Meeting of the Association for Computational Linguistics (Volume 1: Long Papers). pp. 8108–8122. Association for Computational Linguistics (Jul 2023)
15. Hu, E.J., Shen, Y., Wallis, P., Allen-Zhu, Z., Li, Y., Wang, S., Wang, L., Chen, W., et al.: Lora: Low-rank adaptation of large language models. ICLR **1**(2), 3 (2022)

16. Huang, Z., Zhang, X., Zhang, S.: Kiut: Knowledge-injected u-transformer for radiology report generation. In: Proceedings of the IEEE/CVF Conference on Computer Vision and Pattern Recognition. pp. 19809–19818 (2023)
17. Jain, S., Agrawal, A., Saporta, A., Truong, S.Q., Duong, D.N., Bui, T., Chambon, P., Zhang, Y., Lungren, M.P., Ng, A.Y., et al.: Radgraph: Extracting clinical entities and relations from radiology reports. arXiv preprint arXiv:2106.14463 (2021)
18. Jin, H., Che, H., Lin, Y., Chen, H.: Promptmrg: Diagnosis-driven prompts for medical report generation. In: Proceedings of the AAAI Conference on Artificial Intelligence. vol. 38, pp. 2607–2615 (2024)
19. Jing, B., Xie, P., Xing, E.: On the automatic generation of medical imaging reports (2017)
20. Johnson, A.E., Pollard, T.J., Berkowitz, S.J., Greenbaum, N.R., Lungren, M.P., Deng, C.y., Mark, R.G., Horng, S.: Mimic-cxr, a de-identified publicly available database of chest radiographs with free-text reports. Scientific data **6**(1), 317 (2019)
21. Kang, W., Galim, K., Zeng, Y., Lee, M., Koo, H.I., Cho, N.I.: State-offset tuning: State-based parameter-efficient fine-tuning for state space models (2025)
22. Li, K., Daniels, J., Liu, C., Herrero, P., Georgiou, P.: Convolutional recurrent neural networks for glucose prediction. Journal on Biomedical and Health Informatics (J-BHI) **24**(2), 11 (2020)
23. Li, M., Lin, B., Chen, Z., Lin, H., Liang, X., Chang, X.: Dynamic graph enhanced contrastive learning for chest x-ray report generation. In: Proceedings of the IEEE/CVF Conference on Computer Vision and Pattern Recognition. pp. 3334–3343 (2023)
24. Li, M., Lin, H., Qiu, L., Liang, X., Chen, L., Elsaddik, A., Chang, X.: Contrastive learning with counterfactual explanations for radiology report generation. In: European Conference on Computer Vision. pp. 162–180. Springer (2024)
25. Li, S., Qiao, P., Wang, L., Ning, M., Yuan, L., Zheng, Y., Chen, J.: An organ-aware diagnosis framework for radiology report generation. IEEE Transactions on Medical Imaging **43**(12), 4253–4265 (2024)
26. Lin, C.Y.: Rouge: A package for automatic evaluation of summaries. In: Text summarization branches out. pp. 74–81 (2004)
27. Liu, A., Guo, Y., Yong, J.h., Xu, F.: Multi-grained radiology report generation with sentence-level image-language contrastive learning. IEEE Transactions on Medical Imaging **43**(7), 2657–2669 (2024)
28. Liu, R., Li, M., Zhao, S., Chen, L., Chang, X., Yao, L.: In-context learning for zero-shot medical report generation. In: Proceedings of the 32nd ACM International Conference on Multimedia. pp. 8721–8730 (2024)
29. Liu, Y., Li, G., Lin, L.: Cross-modal causal relational reasoning for event-level visual question answering. IEEE Transactions on Pattern Analysis and Machine Intelligence **45**(10), 11624–11641 (2023)
30. Nicolson, A., Dowling, J., Koopman, B.: Improving chest x-ray report generation by leveraging warm starting. Artificial intelligence in medicine **144**, 102633 (2023)
31. Papineni, K., Roukos, S., Ward, T., Zhu, W.J.: Bleu: a method for automatic evaluation of machine translation. In: Proceedings of the 40th annual meeting of the Association for Computational Linguistics. pp. 311–318 (2002)
32. Rehman, M., Shafi, I., Ahmad, J., Garcia, C.O., Barrera, A.E.P., Ashraf, I.: Advancement in medical report generation: current practices, challenges, and future directions. Medical & Biological Engineering & Computing **63**(5), 1249–1270 (2025)
33. Shi, M., Wang, S., Chen, C.Y., Jain, J., Wang, K., Xiong, J., Liu, G., Yu, Z., Shi, H.: Slow-fast architecture for video multi-modal large language models. arXiv preprint arXiv:2504.01328 (2025)
34. Sîrbu, I., Sîrbu, I.R., Bogojeska, J., Rebedea, T.: Git-cxr: End-to-end transformer for chest x-ray report generation. arXiv preprint arXiv:2501.02598 (2025)

35. Tanida, T., Müller, P., Kaassis, G., Rueckert, D.: Interactive and explainable region-guided radiology report generation. In: Proceedings of the IEEE/CVF Conference on Computer Vision and Pattern Recognition. pp. 7433–7442 (2023)
36. Touvron, H., Martin, L., Stone, K., Albert, P., Almahairi, A., Babaei, Y., Bashlykov, N., Batra, S., Bhargava, P., Bhosale, S., et al.: Llama 2: Open foundation and fine-tuned chat models. arXiv preprint arXiv:2307.09288 (2023)
37. Vedantam, R., Lawrence Zitnick, C., Parikh, D.: Cider: Consensus-based image description evaluation. In: Proceedings of the IEEE conference on computer vision and pattern recognition. pp. 4566–4575 (2015)
38. Wang, F., Du, S., Yu, L.: Hergen: Elevating radiology report generation with longitudinal data. In: European Conference on Computer Vision. pp. 183–200. Springer (2024)
39. Wang, J., Bhalerao, A., He, Y.: Cross-modal prototype driven network for radiology report generation. In: European Conference on Computer Vision. pp. 563–579. Springer (2022)
40. Wang, J., Bhalerao, A., Yin, T., See, S., He, Y.: Camanet: class activation map guided attention network for radiology report generation. IEEE Journal of Biomedical and Health Informatics **28**(4), 2199–2210 (2024)
41. Wang, X., Li, Y., Wang, F., Wang, S., Li, C., Jiang, B.: R2gencsr: Retrieving context samples for large language model based x-ray medical report generation. arXiv preprint arXiv:2408.09743 (2024)
42. Wang, X., Li, Y., Wu, W., et al.: Pre-training on high definition x-ray images: An experimental study. arXiv preprint arXiv:2404.17926 (2024)
43. Wang, X., Wang, F., Li, Y., Ma, Q., Wang, S., Jiang, B., Tang, J.: Cxpmrg-bench: Pre-training and benchmarking for x-ray medical report generation on chexpert plus dataset. In: Proceedings of the Computer Vision and Pattern Recognition Conference. pp. 5123–5133 (2025)
44. Wang, X., Wang, S., Ding, Y., et al.: State space model for new-generation network alternative to transformers: A survey. arXiv preprint arXiv:2404.09516 (2024)
45. Wang, Z., Liu, L., Wang, L., Zhou, L.: Metransformer: Radiology report generation by transformer with multiple learnable expert tokens. In: Proceedings of the IEEE/CVF Conference on Computer Vision and Pattern Recognition. pp. 11558–11567 (2023)
46. Wang, Z., Liu, L., Wang, L., Zhou, L.: R2gengpt: Radiology report generation with frozen llms. Meta-Radiology **1**(3), 100033 (2023)
47. Wu, Y., Huang, I.C., Huang, X.: Token imbalance adaptation for radiology report generation. In: Conference on Health, Inference, and Learning. pp. 72–85. PMLR (2023)
48. Xue, Y., Tan, Y., Tan, L., Qin, J., Xiang, X.: Generating radiology reports via auxiliary signal guidance and a memory-driven network. Expert Systems with Applications **237**, 121260 (2024)
49. Yang, Y., Yu, J., Fu, Z., Zhang, K., Yu, T., Wang, X., Jiang, H., Lv, J., Huang, Q., Han, W.: Token-mixer: Bind image and text in one embedding space for medical image reporting. IEEE Transactions on Medical Imaging **43**(11), 4017–4028 (2024)
50. Yao, Y., Liu, Z., Cui, Z., Peng, Y., Zhou, J.: Selective visual prompting in vision mamba (2024)
51. Ye, J., Xu, H., Liu, H., Hu, A., Yan, M., Qian, Q., Zhang, J., Huang, F., Zhou, J.: mplug-owl3: Towards long image-sequence understanding in multi-modal large language models. arXiv preprint arXiv:2408.04840 (2024)
52. Yin, H., Zhou, S., Wang, P., Wu, Z., Hao, Y.: Kia: Knowledge-guided implicit vision-language alignment for chest x-ray report generation. In: Proceedings of the 31st International Conference on Computational Linguistics. pp. 4096–4108 (2025)
53. Yoshimura, M., Hayashi, T., Maeda, Y.: Mambapeft: Exploring parameter-efficient fine-tuning for mamba (2024)

54. Zhu, L., Liao, B., Zhang, Q., Wang, X., Liu, W., Wang, X.: Vision mamba: Efficient visual representation learning with bidirectional state space model. In: Forty-first International Conference on Machine Learning (2024)
55. Zhu, Q., Mathai, T.S., Mukherjee, P., Peng, Y., Summers, R.M., Lu, Z.: Utilizing longitudinal chest x-rays and reports to pre-fill radiology reports. In: International Conference on Medical Image Computing and Computer-Assisted Intervention. pp. 189–198. Springer (2023)
56. Zhu, Y., Xie, C., Liang, S., Zheng, B., Guo, S.: Focusllava: A coarse-to-fine approach for efficient and effective visual token compression. arXiv preprint arXiv:2411.14228 (2024)